IET Science, Measurement & Technology

Spatiotemporal energy-density distribution of time-reversed electromagnetic fields

Elias Le Boudec[1] | Hamidreza Karami[2] | Nicolas Mora[3] | Farhad Rachidi[1] | Marcos Rubinstein[2] | Felix Vega[4]

[1]Electromagnetic Compatibility Laboratory, Ecole polytechnique fédérale de Lausanne, Lausanne, Switzerland

[2]Institute for Information and Communication Technologies, University of Applied Sciences and Arts Western Switzerland, Yverdon-les-Bains, Switzerland

[3]Department of Electrical and Electronics Engineering, Faculty of Engineering, Universidad Nacional de Colombia - Sede Bogotá, Bogotá, Colombia

[4]Directed Energy Research Center, Technology Innovation Institute, Abu Dhabi, United Arab Emirates

Correspondence
Farhad Rachidi, Electromagnetic Compatibility Laboratory, Ecole polytechnique fédérale de Lausanne, ELL 138 (Bâtiment ELL), Station 11, CH-1015 Lausanne, Switzerland.
Email: farhad.rachidi@epfl.ch

Abstract

Time reversal exploits the invariance of electromagnetic wave propagation in reciprocal and lossless media to localize radiating sources. Time-reversed measurements are back-propagated in a simulated domain and converge to the unknown source location. The focusing time (i.e. the simulation instant at which the fields converge to the source location) and the source location can be identified using field maxima, entropy, time kurtosis, and space kurtosis. This paper analyses the spatial energy-density distribution of time-reversed electromagnetic fields by introducing a convergence metric based on the spatial average and variance of the energy density. It is analytically proven that the proposed metric identifies the focusing time and the source location, with direct links to the source frequency content. The analytical results are verified in a free-space numerical simulation and the proposed metric is then compared to existing ones in a simulated inhomogeneous medium. Next, this metric is applied and compared in an experimental case study to localize electromagnetic interference sources. The proposed metric outperforms existing ones to identify the focusing time and can also be used to locate the source. Finally, because of its tensorial nature, it can handle anisotropic media, opening the door to quantitative analyses of time-reversal focusing in metamaterials.

1 | INTRODUCTION

In the electromagnetic time-reversal cavity, introduced by Carminati et al. [1], a sensor spanning a full solid angle around a source allows to focus electromagnetic fields at the source location. This principle has been applied for both wave focusing and imaging. During the direct-time phase, transient or time-harmonic electromagnetic fields are recorded on the boundary of the domain of interest on a "time-reversal mirror" (e.g. a few monopole antennas on the boundary of a reverberant chamber, as in Ref. [2]). The direct-time source is then removed. During the backward propagation phase, the time-reversed measurements are sent from the time-reversal mirror. Because only a finite number of sensors are available, the resulting fields are

not a perfect copy of their direct-time counterpart. However, at least a local field maximum is observed (e.g. in Ref. [3]) at the (unknown) source location. For imaging problems, the backward propagation is often done in a simulated environment. Contrary to experimental case studies, the electromagnetic fields are available at all sampled points in time and space. A focusing time and location can then be obtained by appropriate metrics.

State-of-the-art metrics to determine the time and location of the field focusing involve determining the local maximum or comparing the maximum to the side lobes [2, 4], computing the entropy of the electric field [5], or its space and time kurtoses [6, 7]. The first two methods might not be appropriate for narrowband signals. Also, the entropy lacks interpretability

for electromagnetic waves. Finally, the field entropy and space kurtosis might suffer from an oscillating behaviour, which makes optimal focusing hard to determine. This paper proposes a new spatial convergence metric based on probability theory and electromagnetic energy density. Our metric differs from the state-of-the-art in that it includes weighted field integrals including the time and space coordinates. As we will see, this offers three main advantages: first, the resulting metric has clear physical interpretations; second, we verify that it predicts fewer false positives than the electric field entropy or kurtoses; third, it directly allows to handle anisotropic case studies. The latter point is central when metamaterials are analysed as homogeneous media with effective anisotropic properties, particularly for super-resolution techniques.

The paper is organized as follows: first, Section 2 introduces the metric alongside necessary definitions; Section 3 then shows the consistency of the proposed metric for the field radiated by an electric dipole; next, Section 4 compares the metric to existing metrics in a numerical case study; Section 5 also applies and compares the proposed metric to an experimental case study; Section 6 discusses and compares all results; finally, Section 7 presents the conclusions of the paper.

2 | DEFINITIONS

We base our metric on the electromagnetic energy density u_{EM}, which describes the density of potential energy carried by the electromagnetic fields. Its instantaneous value at time t and position $\mathbf{r}$ in a homogeneous, isotropic, lossless and passive medium of permittivity ε and permeability μ is given by [8, eq. (6.106)]

$$u_{\mathrm{EM}}(t, \mathbf{r}) = \frac{1}{2}\varepsilon|\mathbf{E}(t, \mathbf{r})|^2 + \frac{1}{2\mu}|\mathbf{B}(t, \mathbf{r})|^2 \quad (1)$$

We write three-dimensional vectors in bold type. The latter equation stems from Poynting's theorem and corresponds to potential energy stored in the electric (first term) and magnetic (second term) fields. The electromagnetic field potential energy is given by a spatial integration of the energy density:

$$U_{\mathrm{EM}}(t) = \iiint_V u_{\mathrm{EM}}(t, \mathbf{r})\mathrm{d}V \quad (2)$$

where V denotes the three-dimensional domain of interest. From this, we define the expected value of a function g with respect to the electromagnetic energy at time t as

$$\langle g \rangle_{\mathrm{EM}}^t \stackrel{\mathrm{def}}{=} \frac{1}{U_{\mathrm{EM}}(t)} \iiint_V g(t, \mathbf{r})u_{\mathrm{EM}}(t, \mathbf{r})\mathrm{d}V \quad (3)$$

This amounts to considering $u_{\mathrm{EM}}(t, \mathbf{r})/U_{\mathrm{EM}}(t)$ as a probability density function in a three-dimensional (spatial) probability space. The expected value can also be seen as a weighted average. We thus call $\langle x \rangle_{\mathrm{EM}}^t$ the average x–coordinate of energy at time t, and similarly for the y and z coordinates. In turn, the energy–location standard deviation σ_{xx}^t for the x coordinate at time t is

$$\left(\sigma_{xx}^t\right)^2 \stackrel{\mathrm{def}}{=} \left\langle \left(x - \langle x \rangle_{\mathrm{EM}}^t\right)^2 \right\rangle_{\mathrm{EM}}^t \quad (4)$$

In general, we define the energy–location covariance matrix Σ_{EM}^t as usual in probability theory:

$$\mathbf{e}_v^\top \Sigma_{\mathrm{EM}}^t \mathbf{e}_u \stackrel{\mathrm{def}}{=} \left\langle \left(u - \langle u \rangle_{\mathrm{EM}}^t\right)\left(v - \langle v \rangle_{\mathrm{EM}}^t\right) \right\rangle_{\mathrm{EM}}^t \quad (5)$$

where $u, v \in \{x, y, z\}$. This corresponds to our definition of the inverse of the "quality of focusing" of electromagnetic fields. The trace of the energy–location covariance matrix defines a scalar aggregate metric

$$(\sigma^t)^2 \stackrel{\mathrm{def}}{=} \mathrm{Tr}\left(\Sigma_{\mathrm{EM}}^t\right) = \left(\sigma_{xx}^t\right)^2 + \left(\sigma_{yy}^t\right)^2 + \left(\sigma_{zz}^t\right)^2 \quad (6)$$

The entries of the energy–location covariance matrix Σ_{EM}^t (e.g. $(\sigma_{xx}^t)^2$) allow for a description of the quality of focusing in anisotropic media.

3 | CASE OF AN ELECTRIC DIPOLE

This section applies the metric defined above to a simple theoretical case. In the direct-time phase, we assume that a point dipole of moment $p(t)$ polarized along the z-axis and placed at the origin radiates electromagnetic fields. Far from the source, we record the fields

$$\mathbf{E}_{\mathrm{DT}}(t, \mathbf{r}) = -\mu \sin(\theta)\frac{p'(t - r/c)}{4\pi r}\mathbf{e}_\theta + \mathcal{O}(r^{-2}) \quad (7)$$

$$\mathbf{B}_{\mathrm{DT}}(t, \mathbf{r}) = -\mu \sin(\theta)\frac{p'(t - r/c) + p(t - r/c)c/r}{4\pi cr}\mathbf{e}_\phi \quad (8)$$

where $r = |\mathbf{r}|$, θ and ϕ are the polar and azimuthal angles, c is the speed of light, $\mathcal{O}(r^{-2})$ includes terms asymptotically bounded by r^{-2}, and the (current) dipole moment is given by

$$p(t) = \iiint J_z(t, \mathbf{r})\mathrm{d}V \quad (9)$$

This can be obtained from Ref. [8] by performing inverse Fourier transforms and switching between charge and current moments, thanks to the conservation of charge equation [8, eq. (6.3)].

Next, during the back-propagation phase, the source is removed (indeed, it is unknown in imaging problems), and the fields are propagated from a surface enclosing the region of interest, as in Ref. [1]. The far-field time-reversed fields are thus the sum of a converging and diverging wave:

$$\mathbf{E}_{\mathrm{TR,ff}}(t, \mathbf{r}) = \mu \sin(\theta)\frac{p'(t - r/c) - p'(t + r/c)}{4\pi r}\mathbf{e}_\theta \quad (10)$$
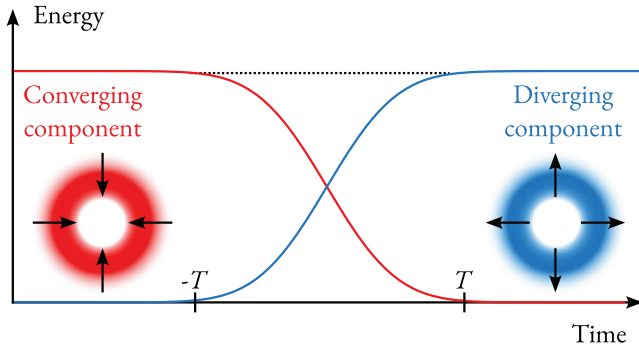
FIGURE 1 Conservation and exchange of energy during the time-reversal operation.

$$\mathbf{B}_{\text{TR,ff}}(t, \mathbf{r}) = \mu \sin(\theta) \frac{p'(t - r/c) + p'(t + r/c)}{4\pi c r} \mathbf{e}_\phi$$
$$+ \mu \sin(\theta) \frac{p(t - r/c) - p(t + r/c)}{4\pi r^2} \mathbf{e}_\phi \quad (11)$$

A Taylor series expansion of a twice continuously differentiable dipole moment p shows that these expressions are regular at the origin. Incidentally, this expansion shows why we did not neglect the $1/r^2$ contribution for the magnetic field. Also, the polarity of the direct-time electric field matches that of the converging wave of the time-reversed field. As explained by Rubinstein et al. [9], the magnetic field is odd under time-reversal symmetry.

In turn, by direct computation from Equation (1), the time-reversed energy density is given by

$$u_{\text{EM}}(t, \mathbf{r}) = \mu \left[\frac{\sin(\theta)}{4\pi c r} \right]^2 \left[p'(t - r/c)^2 + p'(t + r/c)^2 \right] \quad (12)$$

plus terms involving the powers higher than r^{-2}, which we neglect because of the far-field approximation[1]. In this formalism, assuming that the source is only active during the interval $[-T, T]$ for some $T > 0$, it is visible that for $t < T$, the energy is carried by the converging wave alone. For $-T \leq t \leq T$, the energy is absorbed by a point source at the origin and immediately re-emitted by a diverging wave to satisfy energy conservation. Likewise, for $t > T$, the energy is carried by the diverging wave alone. This is illustrated in Figure 1.

We now apply the proposed metric to the derived energy density. The detailed calculations are presented in Appendix A. We show that the average energy–location is the origin (i.e. the source location):

$$\langle \mathbf{r} \rangle_{\text{EM}}^t = \mathbf{0} \quad (13)$$

for all t, which shows the consistency of the proposed metric. Indeed, this shows that the average energy–location can be used

to locate the source location. Furthermore, the energy–location variances for all components x, y and z are convex-quadratic functions of time given by

$$\left(\sigma_{xx}^t \right)^2 = \left(\sigma_{yy}^t \right)^2 = \frac{2c^2}{5} \left[\sigma_s^2 + (t - t_s)^2 \right] \quad (14)$$

$$\left(\sigma_{zz}^t \right)^2 = \frac{c^2}{5} \left[\sigma_s^2 + (t - t_s)^2 \right] \quad (15)$$

where we have introduced the average source–power time

$$t_s \stackrel{\text{def}}{=} \frac{\int_{-\infty}^{\infty} t p'(t)^2 \, dt}{\int_{-\infty}^{\infty} p'(t)^2 \, dt} = \langle t \rangle_{(p')^2} \quad (16)$$

and the source–power variance

$$\sigma_s^2 \stackrel{\text{def}}{=} \left\langle (t - t_s)^2 \right\rangle_{(p')^2} \quad (17)$$

The energy–location variance depends on the source excitation and attains its global minimum at the focusing time $t^\star$, equal to the average source–power time t_s. Indeed, the duration of the source excitation is mirrored in that of the time-reversed fields (longer-duration signals take longer to converge than short-duration signals). Moreover, this metric shows how broadband sources (i.e. with low source–power variance) are more focused than narrowband sources. For example, an impulse-like source (i.e. whose energy is deployed at a single instant)—whose source–power variance is zero—exhibits no energy–location variance. Such a field is, however, an idealization. On the other hand, a purely harmonic signal possesses a high (theoretically infinite) source–power variance and is thus expected to be poorly focused. For such signals, time-domain methods (including the proposed method) might be ill-suited, as they also require long acquisition windows and are well-modelled in the frequency domain by an amplitude and a phase.

In turn, the minimum value of the trace of the energy–location covariance matrix is conveniently given by

$$(\sigma^t)^2 \big|_{t=t^\star} \stackrel{\text{def}}{=} (\sigma^\star)^2 = (c\sigma_s)^2 \quad (18)$$

It becomes apparent that the energy–location variance depends on the speed of light in the medium; slower waves, with reduced wavelengths, focus in a smaller volume.

The energy–location covariance matrix at the focusing time $t^\star$ is given by

$$\Sigma_{\text{EM}}^\star = (c\sigma_s)^2 \begin{bmatrix} \frac{2}{5} & 0 & 0 \\ 0 & \frac{2}{5} & 0 \\ 0 & 0 & \frac{1}{5} \end{bmatrix} \quad (19)$$

More generally, we show in Appendix A that the energy–location covariances are zero for all times. This diagonality results from the dipole being aligned with the z axis; for tilted polarizations, the covariances might be non-zero, but the trace remains constant.

---

[1] As a consequence, the energy density we work with in this section does not correspond to electromagnetic fields near the origin. Indeed, the far-field approximation cannot be directly used to construct time-reversed solutions at the origin—we need to use the complete expressions. However, as we will see in the next section, the derived properties still hold for simulations.

3.1 | Physical interpretation of the proposed metric

There are two main differences between the proposed and existing metrics (see Section 4.1): on the one hand, the proposed metric relies on the energy density, which allows to describe the work carried out by electromagnetic fields on charges—in other words, the interaction between fields and matter. It therefore makes sense to construct a metric based on energy and not the fields themselves. For example, the time-reversed magnetic field in Equation (11) is zero at the origin ($r = 0$), as can be shown by performing a Taylor series expansion. In turn, a metric based solely on the magnetic field would yield irrelevant results. By duality, the same holds for the time-reversed electric field when considering a magnetic dipole.

On the other hand, the proposed metric includes spatially weighted averages of the electromagnetic energy density in the form of the average energy–location and the energy–location variance. As seen above in the theoretical derivation, the average energy–location of time-reversed fields corresponds to the direct-time source location. Physically, this is a consequence of the time-reversal invariance of the wave equation and the design of the time-reversal procedure: the method creates a wavefront converging to the direct-time source location and possessing a rotational symmetry around the polarization axis centred at the source location. This symmetry is mirrored in the energy density and focuses the average energy–location at the source location, ensuring consistency. Simultaneously, most of the fields, and thus most of the energy density, are concentrated around the source location, yielding a low energy–location variance. An analogy is to consider the effect of letting the variance of a Gaussian distribution tend to 0: the density converges (weakly) to a perfectly focused Dirac δ distribution.

3.2 | The effect of the dipole moment

In the theoretical derivation, we neglected high-order contributions to the time-reversed fields. In this section, we first verify numerically that the theoretical results hold for the numerical time-domain simulation of a dipole. To this end, we run a set of two-dimensional (2D) axis-symmetric finite-difference, time-domain (FDTD) simulations using the Meep solver introduced in Oskooi et al. [10]. The simulation domain is a homogeneous, lossless, isotropic and passive medium with a z-polarized dipole source at the origin. We test a smooth, nearly compactly supported asymmetric dipole moment given by

$$p(t) = f''\left[(t - t_0)/\gamma\right] + \frac{1}{2}f''\left[(t - 2t_0)/\gamma\right] \quad \text{in A m} \quad (20)$$

where $f(s) = e^{-s^2}$, $t_0 = 1/f_0$, $\gamma = (\pi f_0)^{-1}$, and f_0 is the main frequency component. This moment is illustrated in Figure 2. We vary the normalized frequencies f_0/c in the range 0.5 to $2\,\text{m}^{-1}$.

To perform the time reversal, we modify the Meep source code to efficiently scale the magnetic fields H and B by a
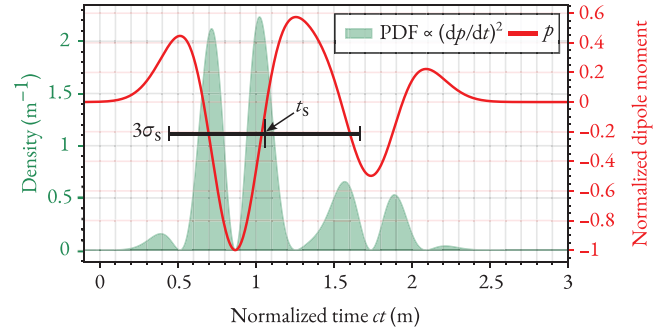

FIGURE 2 The dipole moment $p(t)$ used to validate the proposed metric. The filled graph indicates the source–power-density $(p')^2$. The horizontal line has a length of $3\sigma_s$ and is centred at the average source–power time t_s.
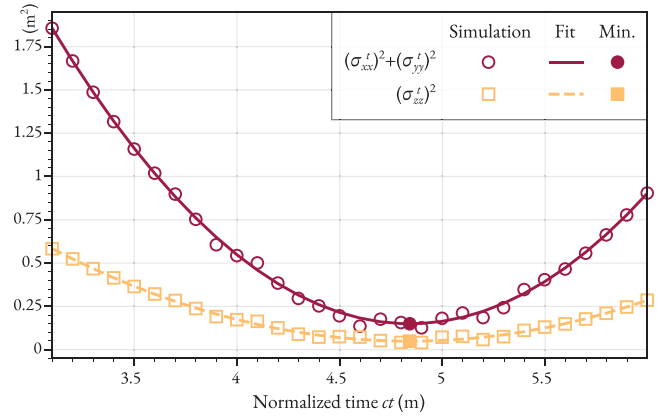

FIGURE 3 Example data used to derive the results in Figure 4 for $f_0/c = 1\,\text{m}^{-1}$. The markers indicate, at each simulation time-step, a numerical computation of the energy–location variance as in Equation (4). Because of the rotational symmetry around the z axis, we combine the xy-plane metrics as $(\sigma_{xx}^t)^2 + (\sigma_{yy}^t)^2$. The quadratic least-squares fit is shown as a solid-and-dashed line. The solid markers indicate the minimum of the fit.

factor -1, thus reversing the Poynting vector. This scaling corresponds to time reversal under two conditions: first, there is no active source and no charge accumulation. Second, the domain is large enough to accommodate the entire signal.

During the time reversal and at each time step, we compute the average energy–locations $\mathbf{r}_0^t$, then the aggregate energy–location standard deviation σ^t from Equation (6). The integrals are approximated using the trapezoidal method on the FDTD grid points. In all simulations, the shape of σ^t as a function of time is nearly quadratic, allowing to determine the optimal focusing-time $t^\star$ and the optimal aggregate energy–location standard deviation $\sigma^\star$ from the coordinates of the minimum of the quadratic fit. An example of such a fit is shown in Figure 3.

The results show that the average energy–location is always the origin, up to numerical errors. As seen in Figure 4, there is an excellent agreement between $t^\star$ and t_s. If a source delivers a delayed signal, we can expect the same from the time-reversed field. Moreover, the energy–location standard deviation $\sigma^\star$ and the source–power standard deviation σ_s match closely. They have the same inverse frequency dependence. Thus, the proposed metric depends on the source–power standard deviation
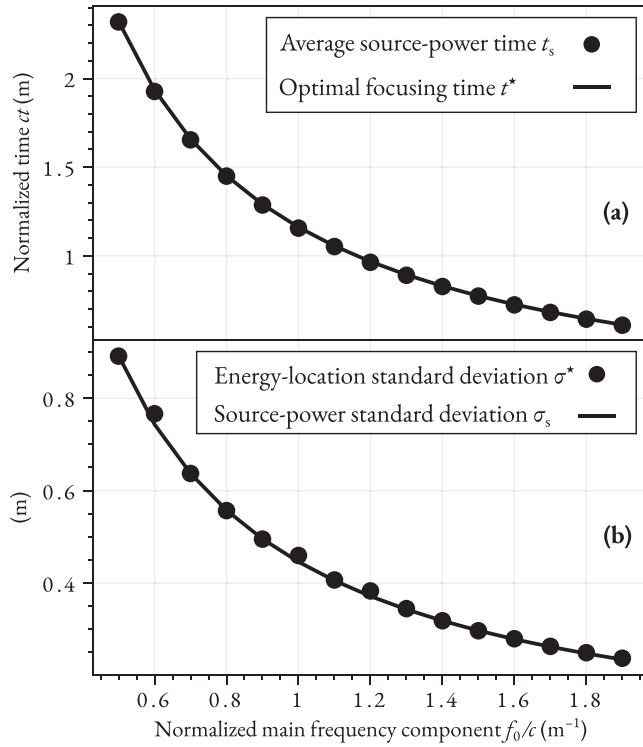
FIGURE 4 FDTD validation of the proposed spatial convergence metric as a function of the normalized main frequency component. (a) Focusing time $t^\star$ given by the simulation and the corresponding average source–power time t_s. (b) Energy–location standard deviation $\sigma^\star$ and source–power standard deviation σ_s.

and average source–power time. As the main frequency component increases, the focusing time and the energy–location standard deviation decrease inversely.

4 | COMPARISON WITH EXISTING CONVERGENCE METRICS

The previous section showed that the proposed metric is consistent (i.e. the average energy–location is the source location), relates the energy–location variance with the source–power variance in the case of a dipole source, and can predict the focusing time. In this section, we apply the proposed metric to a numerical case study and compare it to existing metrics.

4.1 | Time-reversal convergence metrics

We now move to a comparison of the presented metric to existing ones. These metrics yield a time- (resp. space-) dependent quantity, which attains an extremum at the focusing time (resp. source location). The analysis of the fields at the focusing time can also determine the source location.

4.1.1 | Determination of the focusing time

The following metrics can be used to determine the focusing time.

Spatial maximum electric field norm
The maximum of the electric field norm is taken over the simulated (or measured) spatial domain at every point in time:

$$E_{\max}(t) = \max_{\mathbf{r}} |\mathbf{E}(t, \mathbf{r})| \tag{21}$$

This maximum is expected to find a temporal maximum close to the focusing time.

Electric field entropy
The electric field entropy [11], a function of time, is given by

$$S(t) = \frac{\left[\iiint_V |\mathbf{E}(t, \mathbf{r})|^2 \mathrm{d}V\right]^2}{\iiint_V |\mathbf{E}(t, \mathbf{r})|^4 \mathrm{d}V} \tag{22}$$

where V is the spatial domain considered. The entropy is expected to be minimal at the focusing time.

Space kurtosis
Very similar to the electric field entropy, the space kurtosis, introduced by Feng et al. [6], is given by

$$\mathrm{Kurt}(t) = |V| \frac{\iiint_V \left[|\mathbf{E}(t, \mathbf{r})| - \langle|\mathbf{E}|\rangle^t\right]^4 \mathrm{d}V}{\left\{\iiint_V \left[|\mathbf{E}(t, \mathbf{r})| - \langle|\mathbf{E}|\rangle^t\right]^2 \mathrm{d}V\right\}^2} \tag{23}$$

where V is the spatial domain considered, $|V|$ is its volume, and

$$\langle|\mathbf{E}|\rangle^t = \frac{1}{|V|} \iiint_V |\mathbf{E}(t, \mathbf{r})| \mathrm{d}V \tag{24}$$

is the spatial average of the electric field norm at a given time t. It is expected to be maximum at the focusing time.

Energy–location standard deviation
The energy–location standard deviation σ^t, as defined in Equation (6), is expected to be minimized at the focusing time, as shown in the theoretical analysis above.

4.1.2 | Determination of the source location

The following metrics can be used to determine the source location.

Temporal maximum electric field norm
The maximum of the electric field norm is taken over the simulated (or measured) time at every location in space:

$$E_{\max}(\mathbf{r}) = \max_{t} |\mathbf{E}(t, \mathbf{r})| \tag{25}$$

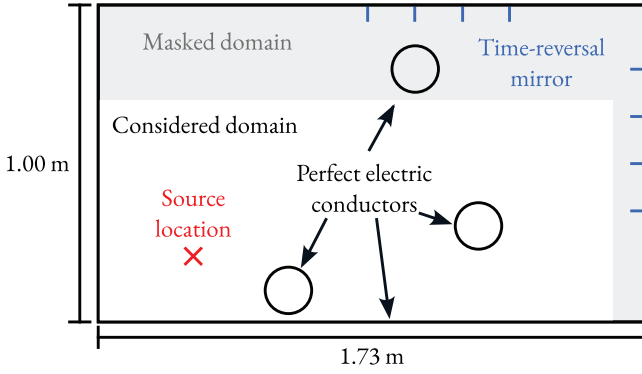This maximum is expected to find a spatial maximum close to the source location.

FIGURE 5 Simulation setup to compare the metrics in inhomogeneous media. A source placed at the marked location radiates in a closed 2D cavity including three spherical scatterers. The fields are recorded and re-emitted from the eight antennas of the time-reversal mirror. The source region is masked and excluded from computations.

Time kurtosis

Feng et al. [7] introduced the time kurtosis of the electric field norm (a function of space):

$$\text{Kurt}(\mathbf{r}) = |T| \frac{\int_T \left[|\mathbf{E}(t,\mathbf{r})| - \langle |\mathbf{E}| \rangle^{\mathbf{r}} \right]^4 \mathrm{d}t}{\left\{ \int_T \left[|\mathbf{E}(t,\mathbf{r})| - \langle |\mathbf{E}| \rangle^{\mathbf{r}} \right]^2 \mathrm{d}t \right\}^2} \quad (26)$$

where T is the time interval considered, $|T|$ is the length of the interval, and

$$\langle |\mathbf{E}| \rangle^{\mathbf{r}} = \frac{1}{|T|} \int_T |\mathbf{E}(t,\mathbf{r})| \mathrm{d}t \quad (27)$$

is the time average of the electric field norm at a given position in space $\mathbf{r}$. The time kurtosis is also expected to be maximal close to the source location.

Average energy–location

The theoretical analysis presented in Section 3 hints towards the use of the average energy–location $\langle \mathbf{r} \rangle_{\text{EM}}^t$ to find the source location. Since this metric depends on time, it is reasonable to consider the average energy–location at the time $t^\star$ where the energy–location standard deviation is minimized. In other words, we expect the source location to be close to $\langle \mathbf{r} \rangle_{\text{EM}}^{t^\star}$.

4.2 | Simulation of inhomogeneous media

In Section 3.2, we verified that the theoretical properties hold in numerical simulations for different dipole moments. We now assess the metric's performance in inhomogeneous media by comparing it to the metrics introduced in the last section. The 2D simulation domain consists of a rectangular metallic cavity including two spherical and metallic scatterers (see Figure 5). A horizontally polarized dipole radiates the second-order derivative of a Gaussian pulse whose main frequency component is 243 MHz. The resulting transient electric field is measured on an eight-channel time-reversal mirror consisting of monopole
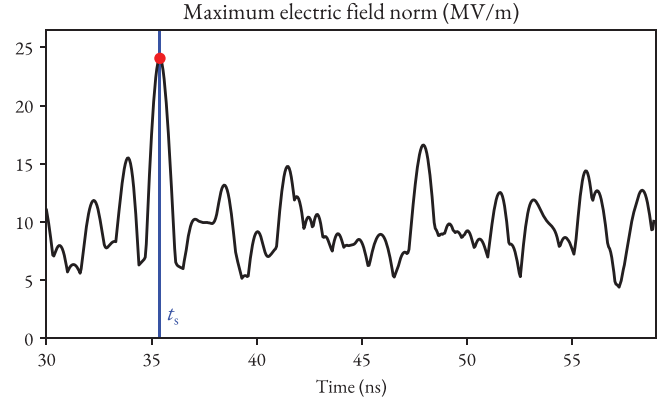

FIGURE 6 Spatial maximum electric field norm as a function of time applied to the 2D inhomogeneous medium case study. The red dot indicates the global maximum.

antennas located as indicated in Figure 5. Four of these antennas are located 13 cm (respectively 30 cm) to the right of (respectively above) the considered domain. Indeed, to avoid biasing the different metrics towards the location of the time-reversal mirror, a region including this mirror is excluded from the computation domain.

Next, the measurements are time-reversed and back-propagated from the time-reversal mirror.

Figures 6–10 present the results obtained using the proposed and the considered existing metrics. The spatial maximum electric field norm (Figure 6) and the energy–location standard deviation (Figure 7(a)) can determine the focusing time. Both the entropy (Figure 8(a)) and the space kurtosis (Figure 9(a)) are minimized or maximized at times where the field is localized (i.e. not spread over the entire domain), but not at the source location (Figure 8(b)). Moreover, the average energy–location is close to the source location (Figure 7(b)). The time kurtosis (Figure 9(b)) and maximum electric field norm (Figure 10) are high at the original location. However, the field enhancement caused by the scatterers introduces spurious local maxima far from the source location.

5 | EXPERIMENTAL VALIDATION

In this section, we compare the proposed metric to existing ones in an experimental setup similar to the one used in Ref. [12]. Contrary to the previous section, the direct-time data is acquired experimentally, and the back-propagation is performed in a simulation.

5.1 | Experimental setup

The experimental setup includes a rectangular cavity with two monopole antennas, each measuring 5.7 cm in length, mounted on a wall of the cavity, as shown in Figure 11. The excitation signal considered in this study is a Gaussian pulse within a frequency range of 0 to 10 GHz, applied to the source antenna
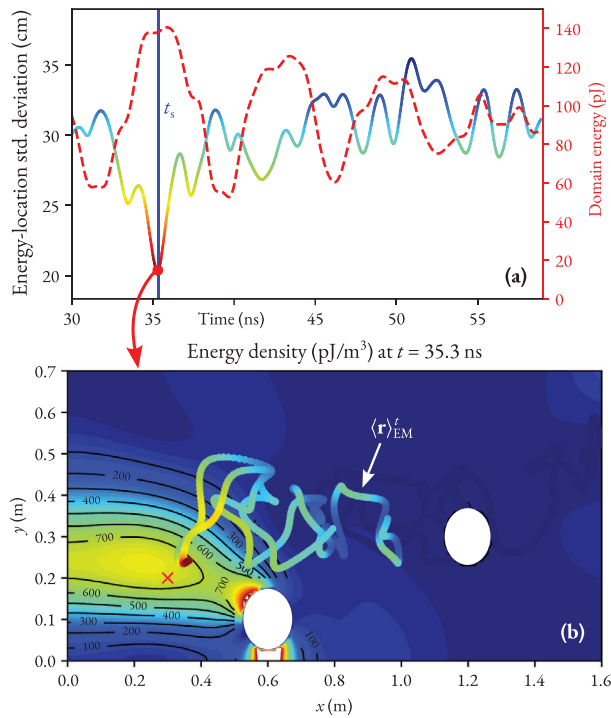
FIGURE 7 Proposed metric applied to a 2D inhomogeneous medium. (a) Energy–location standard deviation as a function of time. The average source–power time is indicated. The dashed line (right-hand side axis) also indicates the domain energy $\iint u_e(t, \mathbf{r})\mathrm{d}S$. The red dot indicates the global minimum, and the energy density at the corresponding time is displayed in (b). In the same plot, the path of the average energy–location at all times is displayed in a colour scheme corresponding to (a).
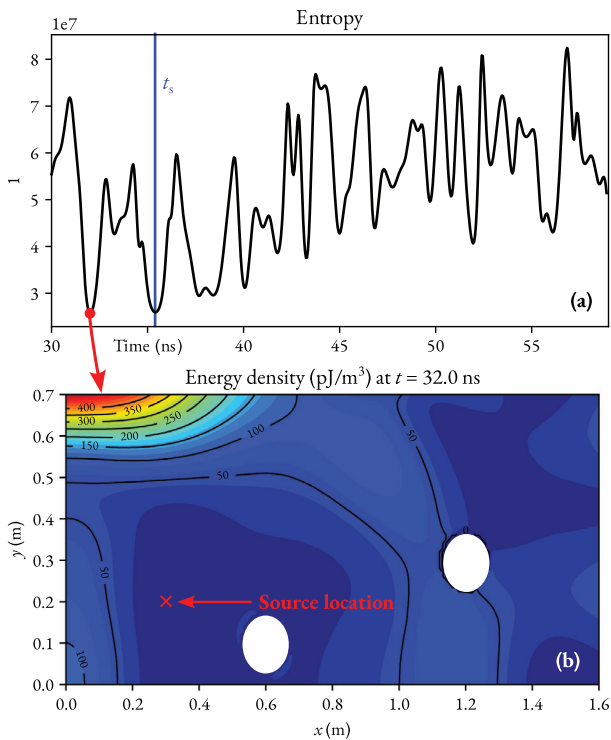

FIGURE 8 Entropy-based metric applied to a 2D inhomogeneous medium. (a) The electric field entropy as a function of time. The red dot indicates the global minimum. (b) plots the energy density distribution at the corresponding time of lowest entropy.
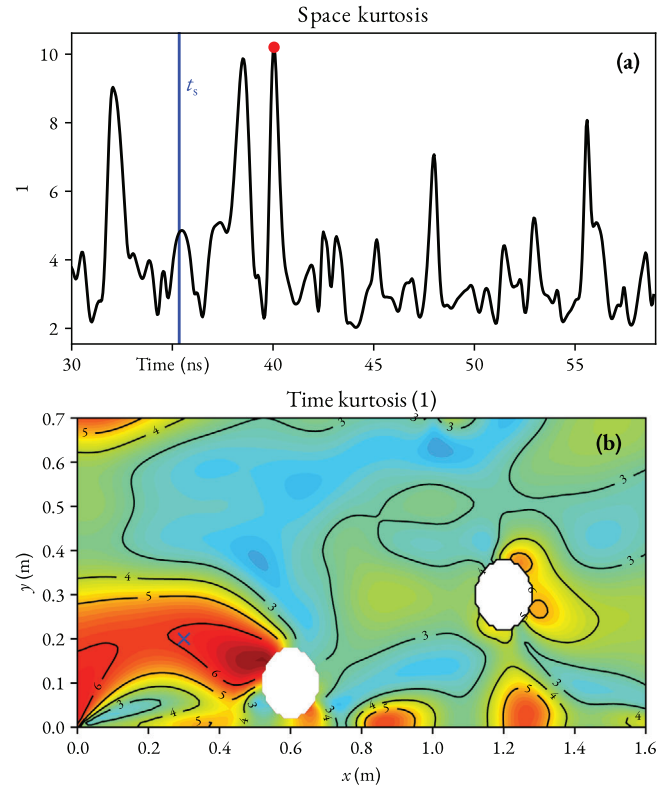

FIGURE 9 Kurtosis-based metrics applied to a 2D inhomogeneous medium. (a) Space kurtosis as a function of time. A red dot indicates the global maximum. (b) Time kurtosis as a function of space. The scatterers correspond to the white ellipses.
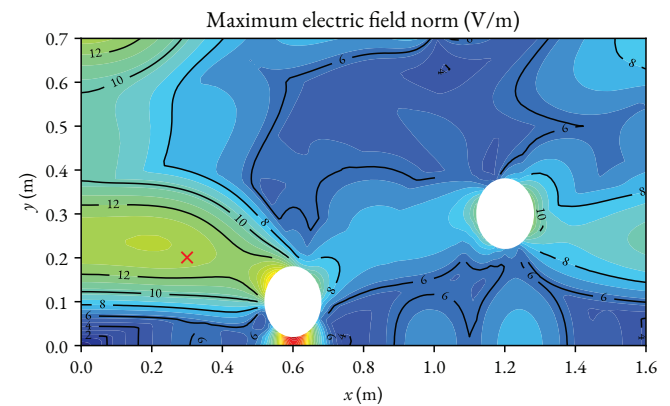

FIGURE 10 Time maximum of the electric field norm applied to the 2D inhomogeneous-medium case study. A red cross indicates the source location.

(lower x–coordinate in Figure 11). To apply the time-reversal method, the frequency response of the cavity between the two monopole antennas is measured using a vector network analyser. Subsequently, to obtain the signal received by the time-reversal mirror, the Fourier transform of the excitation signal is multiplied by the measured frequency response. Finally, an inverse Fourier transform is applied to the result, illustrated in Figure 12. In the backward propagation phase, the geometry of the problem is modelled in CST Studio Suite. The received signal is time-reversed and numerically injected back into the
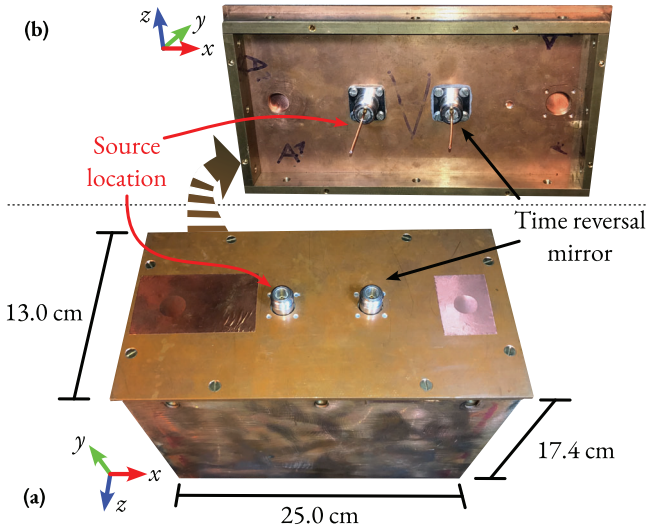
FIGURE 11 Experimental setup. (a) A copper-walled reverberant chamber is fitted with a single-antenna time-reversal mirror. The electromagnetic interference source is introduced by a similar antenna shifted in the negative-x direction. Both antennas are shown in (b).
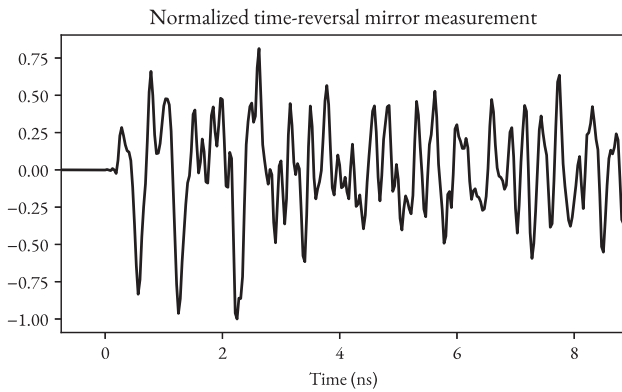

FIGURE 12 Time-domain representation of the signal measured at the time-reversal mirror.

FIGURE 13 Spatial maximum electric field norm as a function of time applied to the 3D experimental case study. The red dot indicates the global maximum.

FIGURE 14 Proposed metric applied to a 3D experimental case study. (a) Energy–location standard deviation as a function of time. The average source–power time is indicated. The dashed line (right-hand side axis) also indicates the domain energy $\iiint u_e(t, \mathbf{r}) \mathrm{d}V$. The red dot indicates the global minimum, and the energy density at the xy-slice at $z = 6.5$ cm and the corresponding time is displayed in (b). In the same plot, the path of the average energy–location at all times is displayed in a colour scheme corresponding to (a).

model from the time-reversal mirror. Then, the metrics presented in Section 4.1 are applied to the simulated electric and magnetic fields. To reduce the effect of the back-propagating antenna near-field, a cylinder around the antenna (illustrated in Figure 16(b)) is excluded from the computation domain.

5.2 | Results

Figures 13–17 present the results obtained using the proposed and the considered existing metrics. Again, the spatial maximum electric field norm (Figure 13) and the energy–location standard deviation (Figure 14(a)) can identify the focusing time. Indeed, the energy density at the corresponding instant (Figure 14(b)) is localized at the source location. Nevertheless, the path described by the average location of energy is contained in a narrow central region, and the source location cannot be identified. As in the simulated case, both the entropy
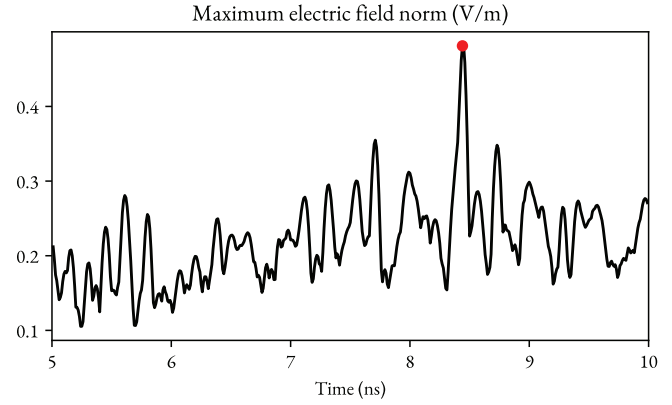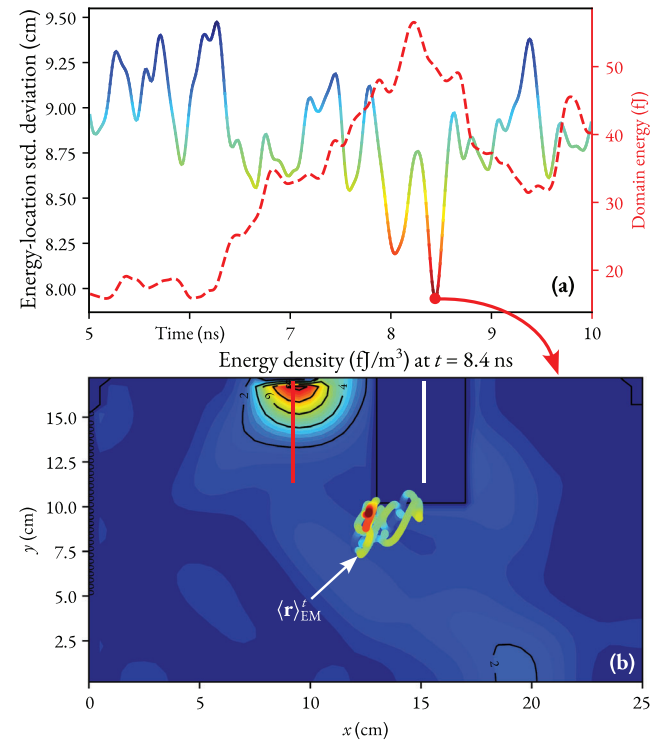
(Figure 15(a)) and the space kurtosis (Figure 16(a)) yield spurious focusing times, as can be seen in Figure 15(b). Also, as seen in Figure 16(b), the time kurtosis is maximal at the source location. However, it also features a spurious local maximum close to the source. Finally, the maximum electric field norm in Figure 17 identifies the source location but also contains many local maxima caused by numerous reflections in the cavity.
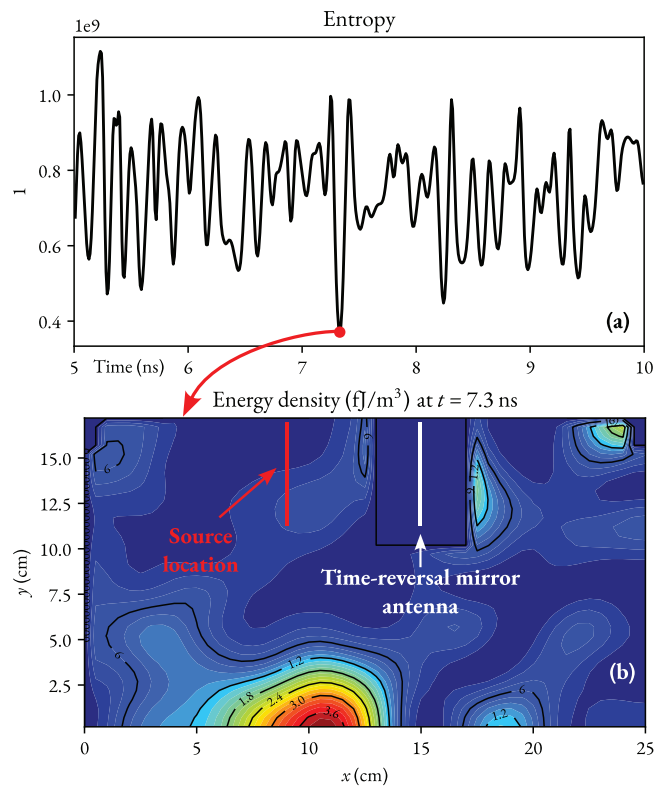
FIGURE 15 Entropy-based metric applied to a 3D experimental case study. (a) The electric field entropy as a function of time. The red dot indicates the global minimum. (b) plots the energy density distribution at the xy-slice at $z = 6.5$ cm and the corresponding time of lowest entropy.
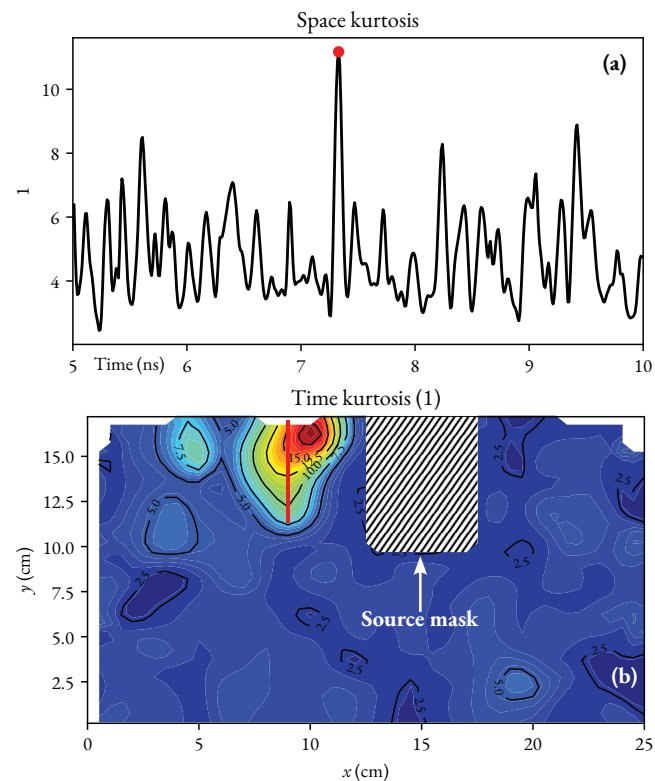

FIGURE 16 Kurtosis-based metrics applied to a 3D experimental case study. (a) Space kurtosis as a function of time. A red dot indicates the global maximum. (b) Time kurtosis as a function of space at the xy-slice at $z = 6.5$ cm.
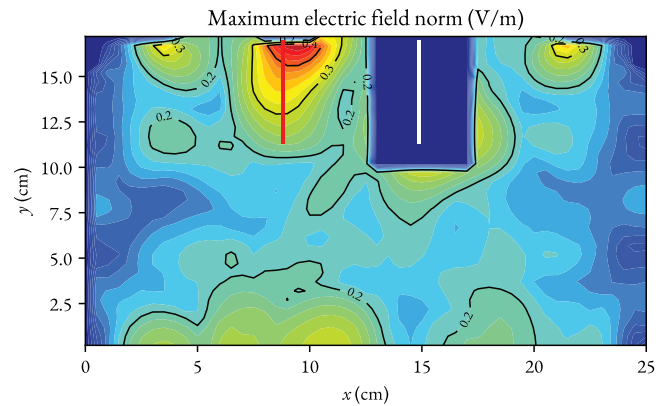

FIGURE 17 Time maximum of the electric field norm applied to a 3D experimental case study. We show the xy-slice at $z = 6.5$ cm.

6 | DISCUSSION

The findings, summarized in Table 1, show that the proposed metric can always determine the focusing time. In the simulated case study, the average energy–location can also estimate the source location. The proximity between the time-reversal mirror and the source can explain the localization failure for the average energy–location metric in the experimental case. Indeed, in this case, the field enhancement induced by the time-reversal mirror antenna attracts the average energy–location. The fact that the total energy is not constant in the considered domain (see Figures 7(a) and 14(a)) might also have an effect. Nevertheless, contrary to other metrics (e.g. the spatial maximum electric field norm, which fares comparably), it is not affected by the field enhancement caused by the scatterers.

Both the experimental and the simulated case studies feature reverberant environments. In reverberation chambers, the typical eigenmode bandwidth (determined by losses) and density (determined by the geometry and frequency) define a threshold for the signal bandwidth, under which mode stirring is usually needed [13]. While the imaging resolution usually increases with bandwidth, as an increasing number of eigenmodes are involved, this increase is however not metric-dependent.

7 | CONCLUSION

In source localization using time reversal, a backward-propagation stage is required to identify the source location. The data from this stage is post-processed to determine the focusing time and source location. Several metrics to quantify this process have been proposed in the literature, including the electric field maximum, the field entropy, time kurtosis, and space kurtosis. We introduced a novel metric based on the spatiotemporal distribution of the electromagnetic energy density. In a theoretical analysis, we showed that the proposed metric can identify the focusing time through the minimum of the energy–location variance (or standard deviation). The focusing time and the minimum energy–location variance (i.e. the best achievable field focusing) can be predicted by the source

TABLE 1 Summary of the metric results in both case studies (simulated 2D inhomogeneous medium and 3D experimental reverberant cavity). In both cases, the time reversal stage is performed in a simulation. We separately assess the metrics' ability to determine the focusing time and the source location. The comparison between the experimental and simulated case studies is irrelevant as the dimensionality, geometries, and source signals differ.

Metric	Inhomogeneous medium case study		Experimental case study	
	Focusing time error (ns)	Source location error (cm)	Focusing time error (ns)	Source location error (cm)
Spatial max. E-field $E_{max}(t)$	0.03	10.4[†,‡]	0.01*	0.6[‡]
Temporal max. E-field $E_{max}(\mathbf{r})$	N/A	10.4[†]	N/A	0.6
Entropy	3.37	58.3[†,‡]	1.10*	16.3[‡]
Space kurtosis	4.68	58.3[†,‡]	1.10*	16.3[‡]
Time kurtosis	N/A	14.9[†]	N/A	1.1
Average energy–location	N/A	7.3	N/A	7.7
Energy–location variance	0.07	7.6[†,‡]	0.01*	0.6[‡]

[†]Ignoring two 20 cm squares centred at the scatterers.
[‡]Obtained by determining the energy density maximum at the focusing time.
*Focusing time reference obtained by visual inspection of the energy density.

excitation waveform through the average source–power time and the source–power variance. We then applied the proposed metric to a numerical case study in inhomogeneous media and compared it to the existing metrics. Finally, we applied the metrics to an experimental case study to locate an electromagnetic interference source.

To conclude, in the studied cases, the focusing time is predicted significantly more reliably by the proposed metric compared to existing ones. This time alone can suffice to determine the source location by observing the field distribution at the corresponding time. The entropy and the kurtosis only consider the statistical distribution of the field values, irrespective of where these values are placed. This lack is filled by the proposed metric, which combines the spatial and temporal information of the field. In applications such as electromagnetic interference source localization, combining several metrics to mitigate the adverse effect of a single metric's disadvantages seems advisable. Finally, the metric allows the study of anisotropic media by considering the entire energy–location covariance matrix (not only its trace). It opens the path to analysing wave focusing in complex media, such as metamaterials.

AUTHOR CONTRIBUTIONS

Elias Le Boudec: Conceptualization; methodology; software; validation; formal analysis; writing—original draft; visualization. **Hamidreza Karami**: Investigation; writing—review & editing. **Nicolas Mora, Farhad Rachidi, Marcos Rubinstein, and Felix Vega**: Writing—review & editing; supervision. **Nicolas Mora, Farhad Rachidi, and Felix Vega**: Project administration; funding acquisition.

CONFLICT OF INTEREST STATEMENT

The authors declare no conflicts of interest.

DATA AVAILABILITY STATEMENT

The data that support the findings of this study are openly available at http://doi.org/10.5281/zenodo.10554616. The soft-

ware used to process the data is available at http://doi.org/10.5281/zenodo.10554953.

ORCID

Elias Le Boudec https://orcid.org/0000-0001-9709-2914
Hamidreza Karami https://orcid.org/0000-0003-0118-6559
Nicolas Mora https://orcid.org/0000-0003-4589-5680
Farhad Rachidi https://orcid.org/0000-0002-2169-9549
Marcos Rubinstein https://orcid.org/0000-0003-4806-038X
Felix Vega https://orcid.org/0000-0001-6854-2971

REFERENCES

1. Carminati, R., Pierrat, R., de Rosny, J., Fink, M.: Theory of the time reversal cavity for electromagnetic fields. Opt. Lett. 32(21), 3107–3109 (2007). https://doi.org/10.1364/OL.32.003107
2. Lemoult, F., Fink, M., Lerosey, G.: Far-field sub-wavelength imaging and focusing using a wire medium based resonant metalens. Waves Random Complex Media 21(4), 614–627 (2011). https://doi.org/10.1080/17455030.2011.613954
3. Lerosey, G., de Rosny, J., Tourin, A., Fink, M.: Focusing beyond the diffraction limit with far-field time reversal. Science 315(5815), 1120–1122 (2007). https://doi.org/10.1126/science.1134824
4. Karami, H., Azadifar, M., Mostajabi, A., Rubinstein, M., Rachidi, F.: Localization of electromagnetic interference source using a time reversal cavity: application of the maximum power criterion. In: 2020 IEEE International Symposium on Electromagnetic Compatibility Signal/Power Integrity (EMCSI), pp. 598–602. IEEE, Piscataway, NJ (2020)
5. Xu, X., Miller, E.L., Rappaport, C.M.: Minimum entropy regularization in frequency-wavenumber migration to localize subsurface objects. IEEE Trans. Geosci. Remote Sens. 41(8), 1804–1812 (2003). https://doi.org/10.1109/TGRS.2003.813497
6. Feng, X.Y., Chen, Z., Xu, Z.M.: Time-reversal source reconstruction with electromagnetic kurtosis. IEEE Trans. Antennas Propag. 69(10), 6816–6823 (2021). https://doi.org/10.1109/TAP.2021.3069523
7. Feng, X.Y., Chen, Z., Xu, Z.M., Li, J.: Time-reversal source reconstruction with space and time kurtoses. IEEE Trans. Antennas Propag. 70(6), 4766–4773 (2022). https://doi.org/10.1109/TAP.2021.3137384
8. Jackson, J.D.: Classical Electrodynamics, 3rd edn. Wiley, New York (1999)
9. Rubinstein, M., Rachidi, F., Paolone, M.: Time reversal: a different perspective. In: Electromagnetic Time Reversal, pp. 1–27. Wiley, New York (2017)
10. Oskooi, A.F., Roundy, D., Ibanescu, M., Bermel, P., Joannopoulos, J.D., Johnson, S.G.: Meep: a flexible free-software package for electromagnetic

simulations by the FDTD method. Comput. Phys. Commun. 181(3), 687–702 (2010). https://doi.org/10.1016/j.cpc.2009.11.008

11. Wiggins, R.A.: Minimum entropy deconvolution. Geoexploration 16(1), 21–35 (1978). https://doi.org/10.1016/0016-7142(78)90005-4

12. Karami, H., Azadifar, M., Mostajabi, A., Favrat, P., Rubinstein, M., Rachidi, F.: Localization of electromagnetic interference sources using a time-reversal cavity. IEEE Trans. Ind. Electron. 68(1), 654–662 (2021). https://doi.org/10.1109/TIE.2019.2962460

13. Crawford, M.L., Koepke, G.H.: Design, Evaluation, and Use of a Reverberation Chamber for Performing Electromagnetic Susceptibility/Vulnerability Measurements. U.S. Department of Commerce, Washington, D.C. (1986)

APPENDIX A: ENERGY–LOCATION COVARIANCE OF A DIPOLE

In this appendix, we look at the time dependence of the proposed metric in the case of a time-reversed dipole, yielding the results presented in Section 3.

We first compute the energy $U_{EM}(t)$ in spherical coordinates, from Equation (12):

$$U_{EM}(t) = \frac{\mu}{(4\pi c)^2} \int_0^\infty \left[p'(t - r/c)^2 + p'(t + r/c)^2 \right] dr$$
$$\int_0^\pi \sin^3(\theta) d\theta \int_0^{2\pi} d\phi \quad (A1)$$

to get

$$\int_0^\infty \left[p'(t - r/c)^2 + p'(t + r/c)^2 \right] dr = \frac{6\pi c^2}{\mu} U_{EM}(t) \quad (A2)$$

By performing the integral separately on both terms of the integrand above, together with the changes of variable $u = t \mp r/c$, we see that $U_{EM}(t)$ does not depend on the time t. We thus write U_{EM} from now on.

Next, let us compute the average energy–location. By rotational symmetry around the z-axis, $\langle x \rangle_{EM}^t = \langle y \rangle_{EM}^t$; we thus focus on

$$\langle x \rangle_{EM}^t = \frac{\mu}{U_{EM}(4\pi c)^2} \int_0^\infty \left[p'(t - r/c)^2 + p'(t + r/c)^2 \right] dr$$
$$\int_0^\pi \sin^4(\theta) d\theta \int_0^{2\pi} \cos(\phi) d\phi = 0 \quad (A3)$$

Likewise,

$$\langle z \rangle_{EM}^t = \frac{\mu}{U_{EM}(4\pi c)^2} \int_0^\infty \left[p'(t - r/c)^2 + p'(t + r/c)^2 \right] dr$$
$$\int_0^\pi \sin^3(\theta) \cos(\theta) d\theta \int_0^{2\pi} d\phi = 0 \quad (A4)$$

In summary, the average energy–location is the origin, i.e. $\langle \mathbf{r} \rangle_{EM}^t = \mathbf{0}$ for all t.

We turn our attention to the energy–location variance. We have

$$(\sigma_{xx}^t)^2 = \langle x^2 \rangle_{EM}^t - \underbrace{(\langle x \rangle_{EM}^t)^2}_{0} \quad (A5)$$

As above,

$$(\sigma_{xx}^t)^2 = \frac{\mu}{U_{EM}(4\pi c)^2} \int_0^\infty r^2 \left[p'(t - r/c)^2 + p'(t + r/c)^2 \right] dr$$
$$\int_0^\pi \sin^5(\theta) d\theta \int_0^{2\pi} \cos^2(\phi) d\phi$$
$$= \frac{\mu}{15\pi c^2 U_{EM}} \int_0^\infty r^2 \left[p'(t - r/c)^2 + p'(t + r/c)^2 \right] dr \quad (A6)$$

We now show that this is a convex quadratic function of time. To this end, we calculate the time derivatives by differentiating under the integral sign:

$$\frac{d(\sigma_{xx}^t)^2}{dt} = \frac{2\mu}{15\pi c^2 U_{EM}} \cdot$$
$$\int_0^\infty r^2 \underbrace{\left[p'(t - r/c)p''(t - r/c) + p'(t + r/c)p''(t + r/c) \right]}_{\partial_r \left[-c/2 p'(t-r/c)^2 + c/2 p'(t+r/c)^2 \right]} dr$$
$$= \frac{2\mu}{15\pi c U_{EM}} \int_0^\infty r \left[p'(t - r/c)^2 - p'(t + r/c)^2 \right] dr \quad (A7)$$

by integration by parts and the support of p. Further differentiating,

$$\frac{d^2(\sigma_{xx}^t)^2}{dt^2} = \frac{4\mu}{15\pi c U_{EM}} \cdot$$
$$\int_0^\infty r \underbrace{\left[p'(t - r/c)p''(t - r/c) - p'(t + r/c)p''(t + r/c) \right]}_{\partial_r \left[-c/2 p'(t-r/c)^2 - c/2 p'(t+r/c)^2 \right]} dr$$
$$= \frac{2\mu}{15\pi U_{EM}} \int_0^\infty \left[p'(t - r/c)^2 + p'(t + r/c)^2 \right] dr = \frac{4c^2}{5} > 0 \quad (A8)$$

by Equation (A2). Similarly, for the z-component, we obtain

$$\frac{d^2 (\sigma_{zz}^t)^2}{dt^2} = \frac{2c^2}{5} > 0 \qquad (A9)$$

Therefore, the energy–location variance for the x, y, and z components is a convex-quadratic function of time. It reaches its global minimum at some time $t^\star$ satisfying, by Equation (A7),

$$\frac{d(\sigma_{xx}^t)^2}{dt} = 0 \iff \int_0^\infty r\big[p'(t^\star - r/c)^2 - p'(t^\star + r/c)^2\big]dr = 0$$

$$\iff \int_0^\infty rp'(t^\star - r/c)^2 dr = \int_0^\infty rp'(t^\star + r/c)^2 dr \qquad (A10)$$

By the changes of variable $u = t^\star \mp r/c$, the criterion becomes

$$\int_{-\infty}^{t^\star} (t^\star - u)p'(u)^2 du = \int_{t^\star}^\infty (u - t^\star)p'(u)^2 du$$

$$\iff t^\star \int_{-\infty}^\infty p'(u)^2 du = \int_{-\infty}^\infty up'(u)^2 du \qquad (A11)$$

$$\iff t^\star = \frac{\int_{-\infty}^\infty tp'(t)^2 dt}{\int_{-\infty}^\infty p'(t)^2 dt} = t_s = \langle t \rangle_{(p')^2} \qquad (A12)$$

by grouping integrals. We also recognized the expected value of t given the density $(p')^2$, i.e. the average source–power time t_s. Note that this time $t^\star$ is the same for all coordinates.

Finally, the minimum energy–location variance is obtained by evaluating Equation (A6) at the time $t^\star$ obtained above:

$$(\sigma_{xx}^\star)^2 = \frac{\mu}{15\pi c^2 U_{EM}} \int_0^\infty r^2 \big[p'(t^\star - r/c)^2 + p'(t^\star + r/c)^2\big]dr$$

$$= \frac{\mu c}{15\pi U_{EM}} \left[\int_{-\infty}^{t^\star} (t^\star - u)^2 p'(u)^2 du + \int_{t^\star}^\infty (u - t^\star)^2 p'(u)^2 du \right]$$

$$= \frac{\mu c}{15\pi U_{EM}} \int_{-\infty}^\infty (u - t^\star)^2 p'(u)^2 du \qquad (A13)$$

where we performed the changes of variable $u = t \mp r/c$ and regrouped the resulting integrals. Again, we recognize a variance in terms of source power:

$$(\sigma_{xx}^\star)^2 = \frac{\mu c}{15\pi U_{EM}} \sigma_s^2 \int_{-\infty}^\infty p'(t)^2 dt \qquad (A14)$$

For some $t_0 > T$, the total energy is given by the outgoing component alone:

$$U_{EM} = \frac{\mu}{(4\pi c)^2} \int_0^\infty p'(t_0 - r/c)^2 dr \int_0^\pi \sin^3(\theta)d\theta \int_0^{2\pi} d\phi$$

$$= \frac{\mu}{6\pi c} \int_{-\infty}^{t_0} p'(t)^2 dt = \frac{\mu}{6\pi c} \int_{-\infty}^\infty p'(t)^2 dt \qquad (A15)$$

by the change of variable $t = t_0 - r/c$ and because $t_0 > T$. Introducing into Equation (A14), we obtain

$$(\sigma_{xx}^\star)^2 = (\sigma_{yy}^\star)^2 = \frac{2c^2}{5} \sigma_s^2 \qquad (A16)$$

Similarly, for the z component,

$$(\sigma_{zz}^\star)^2 = \frac{c^2}{5} \sigma_s^2 \qquad (A17)$$

Finally, it is straightforward to check from Equation (A6) that the covariances are zero for all t, i.e.

$$\langle xy \rangle_{EM}^t = \langle xz \rangle_{EM}^t = \langle yz \rangle_{EM}^t = 0 \qquad (A18)$$